Solution Spraying of Poly(methyl methacrylate) Blends to Fabricate Micro-textured, Superoleophobic Surfaces

Siddarth Srinivasan[a], Shreerang S. Chhatre[a], Joseph M. Mabry[b], Robert E. Cohen[a] and Gareth H. McKinley[c]

[a] Department of Chemical Engineering, Massachusetts Institute of Technology, Cambridge 02139

[b] Space and Missile Propulsion Division, Air Force Research Laboratory, Edwards Air Force Base, California 93524

[c] Department of Mechanical Engineering, Massachusetts Institute of Technology, Cambridge 02139

Corresponding Authors: Tel.: (617) 253-3777 (R.E.C.); (617) 258-0754 (G.H.M.). Email.; recohen@mit.edu (R.E.C); gareth@mit.edu (G.H.M).

ABSTRACT

We describe a simple technique to prepare superhydrophobic and superoleophobic micro-textured surfaces by spray coating a blend of poly(methyl methacrylate) (PMMA) and the low surface energy molecule 1H,1H,2H,2H-heptadecafluorodecyl polyhedral oligomeric silsesquioxane (fluorodecyl POSS, $\gamma_{sv} \approx 10$ mN/m) using an air brush with a pressurized nitrogen stream. Scanning electron micrographs show the formation of micro-textured surfaces possessing re-entrant curvature; a critical feature for obtaining liquid repellency with low surface tension liquids. The surface morphology can be tuned systematically from a corpuscular or spherical microstructure to a beads-on-string structure and finally to bundled fibers by controlling the solution concentration and molecular weight of the sprayed polymer. The oleophobicity of the resulting structures is characterized by advancing and receding contact angle measurements with liquids of a range of surface tensions.

KEYWORDS

non-woven; fiber; superhydrophobic; superoleophobic; spray coating; beads on string;

I. Introduction

The production of micrometer and sub-micrometer sized nonwoven meshes/mats, coupled with the ability to tailor the morphological properties, is of interest in a number of applications including sensors, filtration, drug release, tissue engineering scaffolds, and liquid repellent fabrics [1-5]. Nonwoven fabrics and filter meshes are produced primarily by melt spinning, melt blowing and electrospinning processes. In melt spinning, a polymer melt is extruded through a spinneret and is taken up at a higher velocity downstream by a draw roll, and the resulting tensile stress draws the melt into fibers of average diameter from 2-10 μm at high production rates [6, 7]. Melt blowing is a modification of this process in which the extruded molten polymer is drawn at higher temperatures by an external jet of hot air resulting in fibers of 0.5-2 μm [8]. In contrast, electrospinning involves the application of a strong electrostatic field to accelerate a polymer solution jet at room temperatures, again producing very fine (submicron) fibers. The electrospinning process is limited by the slow rate of fiber production, and it requires adequate conductivity of the polymer jet. The need for a high voltage source adds to the cost and complexity of the process [3, 8, 9].

Spray deposition is an alternative low cost technique to rapidly and conformally coat large areas on a variety of substrates. Medeiros *et al* [10] developed a "solution blow spinning" technique to produce fibers with diameters of 1μm and smaller from a polymer solution by using a syringe pump to deliver the solution through a nozzle into a high velocity gas flow. We describe a similar simple spraying technique to fabricate various microtextured surfaces from a polymer solution containing a perfluorinated dispersant, with the ability to control the morphology from fibers to beads-on-string and corpuscular structures. The incorporation of the low surface energy 1H,1H,2H,2H-heptadecafluorodecyl polyhedral oligomeric silsesquioxane (fluorodecyl POSS) cage molecule in the polymer solution confers these microtextured surfaces with significantly enhanced liquid repellent properties.

The fabrication of surfaces and coating techniques which promote low surface tension liquid repellency have a number of potential applications, including fabrics with resistance to wetting by oils, surface coatings for reducing biofouling or fluid frictional drag and separation of oil/water

dispersions. Superhydrophobic surfaces - which exhibit a contact angle of $\theta^* > 150^\circ$ and low contact angle hysteresis with water – have been prepared by a number of techniques including lithography [11], sol-gel processing [12], electrospinning [13], electrodeposition [14] and chemical vapor deposition [15]. Similar techniques that enable the preparation of more complex textured surfaces with the locally re-entrant topography needed to promote superoleophobic behavior when in contact with low surface tension liquids have also been reported [16-25]. These techniques result in a low energy micro-patterned re-entrant surface that can support the composite air/liquid interface characteristic of a super-repellent surface, but are usually expensive, involve multiple processing steps or are difficult to scale up to coat large substrate areas. There is a need to develop processing techniques that enable preparation of robust liquid-repellent surfaces using a simple, rapid and scalable process. A few nanocomposite spray coating methods to produce superhydrophobic surfaces have been reported [26-30]. Steele *et al* [31] have described a technique to fabricate superoleophobic surfaces by spray casting ZnO nanoparticles blended with a waterborne perfluroacrylic polymer emulsion using volatile cosolvents followed by curing. In this article, we present an alternate technique to fabricate superoleophobic surfaces in a single step process by solution spraying of polymethyl methacrylate (PMMA) and fluorodecyl POSS blends dissolved in the hydrochlorofluorocarbon solvent Asahiklin AK-225, under a pressurized nitrogen stream.

The wettability of liquids on solid surfaces is governed by the chemical composition of the surface as well as the topographic texture and roughness at the micro/nano-length scales [32-35]. For a smooth homogenous surface with an equilibrium contact angle θ_E, the presence of surface roughness is known to influence the wettability by two alternative mechanisms; in the Wenzel model [36], the roughness (r) increases the surface area of the wetted solid in contact with the liquid drop and influences the observed contact angle (θ^*) according to the equation $\cos\theta^* = r\cos\theta$. By contrast, in the Cassie-Baxter [37] model, pockets of air are trapped between the liquid drop and the solid substrate and this modifies the apparent contact angle through an expression of the form

$$\cos\theta^* = r_\phi \phi_s \cos\theta_E + \phi_s - 1 \qquad (1)$$

where r_ϕ is the roughness of the wetted area, ϕ_s is the area fraction of the liquid-air interface occluded by the solid texture, and $r_\phi \phi_s$ is the fraction of the solid substrate in contact with the liquid [38]. A thermodynamic free energy analysis for a specific liquid on a textured solid surface can be used to predict which of these two possible states is the equilibrium wetting state [38, 39]. For liquids with low surface tensions the local surface curvature and topography of the surface texture

has been shown to be a crucial parameter in supporting metastable Cassie-Baxter states and enabling the rational design of oleophobic surfaces [17, 18, 22, 23].

II. Materials and Methods

Low surface energy fluorodecyl POSS molecules ($\gamma_{sv} \approx 10$ mN/m), whose synthesis technique has been previously reported [40], were mixed with PMMA to form solutions of various concentrations using the commercially available hydrofluorocarbon solvent Asahiklin AK-225 (Asahi Glass Company, bp: 54° C), which consists of 3,3-dichloro-1,1,1,2,2-pentafluoropropane (HCFC-225ca) and 1,3-dichloro-1,1,1,2,3-pentafluoropropane (HCFC-225cb). To investigate the roles of chain length and polydispersity on the textures produced by the spraying process, a number of different PMMA samples have been studied. Each sample used to prepare the solution was first characterized using Gel Permeation Chromatography (GPC), and the corresponding molecular weights and polydispersity are summarized in Table 1. In particular, two different molecular weight samples of polydisperse PMMA (B1,B2; Scientific Polymer Products) have been studied, and characterization with GPC showed these have a weight averaged molecular weight (M_w) and polydispersity index (*PDI*) of B1: M_w=102,000 g/mol, *PDI*=1.56 and B2: M_w=593,000 g/mol, *PDI*=2.69 respectively. These two polydisperse samples are contrasted with a range of monodisperse PMMA fractions (N1,N2,N3; Pressure Chemical Company, N4; Sigma-Aldrich) which were used to prepare a series of model solutions that enable us to characterize the role of polymer molecular weight on sprayed surface morphology. In Figure 1, we show the GPC curves using DMF as the solvent of four different narrow PMMA standards (N1: M_w=124,000 g/mol, *PDI*=1.04; N2: M_w=272,000 g/mol, *PDI*=1.11; N3: M_w=761,000 g/mol, *PDI*=1.13; N4: M_w=2,276,000 g/mol, *PDI*=1.08), along with the broad polydisperse samples (B1,B2). The molecular weight distributions of the PMMA standards are observed to be fairly monodisperse as expected with PDI < 1.2 for all samples. The high molecular weight monodisperse PMMA sample (N4) was also used in supplemental experiments to determine sprayability at very low concentrations.

Table 1. The number average molecular weight (M_n), weight average molecular weight (M_w), the peak molecular weight (M_p) and the polydispersity index ($\mathrm{PDI} = M_w/M_n$) of the PMMA samples used in preparing solutions for spraying.

PMMA samples	$M_n\left(\times 10^3\right)$ (g/mol)	$M_w\left(\times 10^3\right)$ (g/mol)	$M_p\left(\times 10^3\right)$ (g/mol)	PDI M_w/M_n
B1	65	102	82	1.56
B2	220	593	721	2.69
N1	118	124	125	1.04
N2	245	272	247	1.11
N3	565	761	605	1.13
N4	2117	2276	2580	1.08

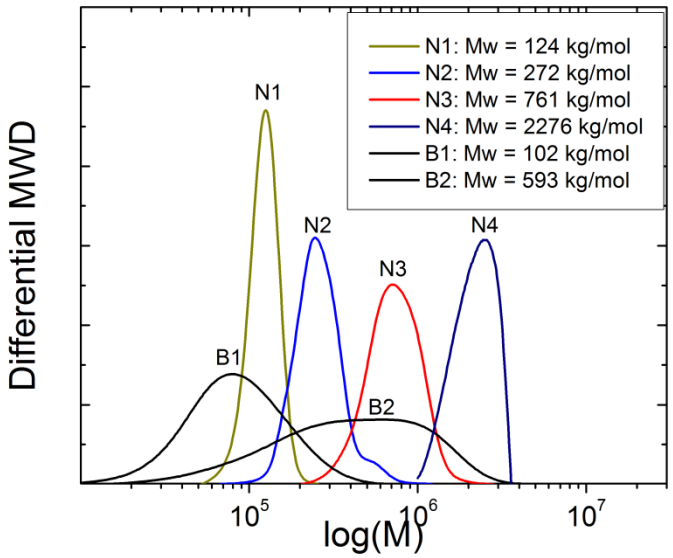

Figure 1. GPC curves for PMMA samples dissolved in dimethylformamide showing the normalized differential molecular weight distribution $\left(dW(M)/d\log M\right)$ against the molecular weight $\left(M\right)$. Four PMMA standards with narrow distributions and low polydispersity (N1,N2,N3,N4) are used to prepare solutions for spraying along with two broad PMMA samples (B1,B2).

An air brush (McMaster-Carr) with a nozzle diameter of 0.75 mm was connected to a compressed nitrogen tank (pressure P=170 kPa) to spray coat the polymer solution at a distance of $l = 20$ to 30 cm onto the substrate (Figure 2). It was observed that the variation of the spraying distance within this range did not have a significant effect on the microtexture obtained, and we focus in this article on a single spraying distance of $l = 25$ cm. The air brush was held fixed during the spraying process. The diameter covered by the conical spray jet at the substrate over the duration of the spraying was ~ 7 cm in diameter, while the size of the silicon wafer was 2 cm x 2 cm.

Contact angle measurements to characterize the surface wettability were performed using a VCA 2000 (AST, Inc.) and a Rame-Hart Model 590 goniometer. The advancing $\left(\theta^*_{adv}\right)$ and receding $\left(\theta^*_{rec}\right)$ contact angles were measured via the sessile drop technique upon adding and removing a total volume ~ 10-15 μL of each liquid, forming a drop with maximum diameter of ~ 2.5 *mm,*

averaged over different locations on the coated substrate. The sliding angles were measured independently by tilting the stage until incipient motion of the droplet was detected. A JSM-6060 Scanning Electron Microscope (JEOL) was used to characterize the surface morphology of each sprayed texture, sputter-coated with gold, under an operating voltage of 5kV. Energy-Dispersive X-ray Spectroscopy (EDX) was performed using a XL30 FEG Enviromental Scanning Electron Microscope (FEI/Philips). The shear viscosities of the polymer/fluoroPOSS solutions were measured with an AR-G2 rheometer (TA Instruments) using a double-gap couette geometry.

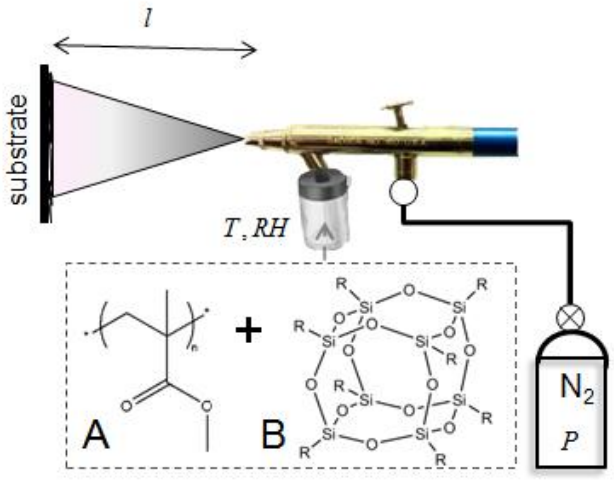

Figure 2. Schematic of spray apparatus and the chemical structure of PMMA (*A*) and the FluoroPOSS cage molecule (*B*, R = -CH_2-CH_2-$(CF_2)_7$-CF_3) sprayed at a distance l = 25cm and pressure P = 170 kPa under a constant temperature and a range of relative humidity (T = 21.6 °C, *RH*: 20-60 %).

III. Results and Discussion

The solution concentration and molecular weight of the dissolved polymer are critical in controlling the morphological characteristics of the micro-textured surfaces generated using this simple spraying process. To demonstrate this, we use three different POSS/PMMA solutions (B2; Mw=593k, PDI=2.69) with solute concentrations (15, 25 and 50 mg/ml) at a fixed fraction of 50 wt% flurodecyl POSS, and the duration of spraying was controlled to ensure that the total mass of the polymer blend delivered to each surface remained constant. At relatively low solute concentrations (15 mg/ml), the silicon substrate is completely covered by a corpuscular layer of spherical microbeads (~ 20 μm diameter). At a higher solute concentration of 25 mg/ml, a transition to a beads-on-string morphology is seen with individual fibrous strands of diameter < 1

μm and beads of diameter ranging from 20 μm – 50 μm. At higher solute concentrations (50 mg/ml) a dense fibrous mesh is produced, with individual strands forming bundles of locally oriented fibers. The texture composed of corpuscular structures was found to exhibit slightly higher advancing and receding contact angles when compared to the bundled fibers. This is consistent with previous work by Ma *et al* [41] and Tuteja *et al* [23] who report higher contact angles for bead-like electrospun surfaces when compared with bead free electrospun surfaces of fibers.

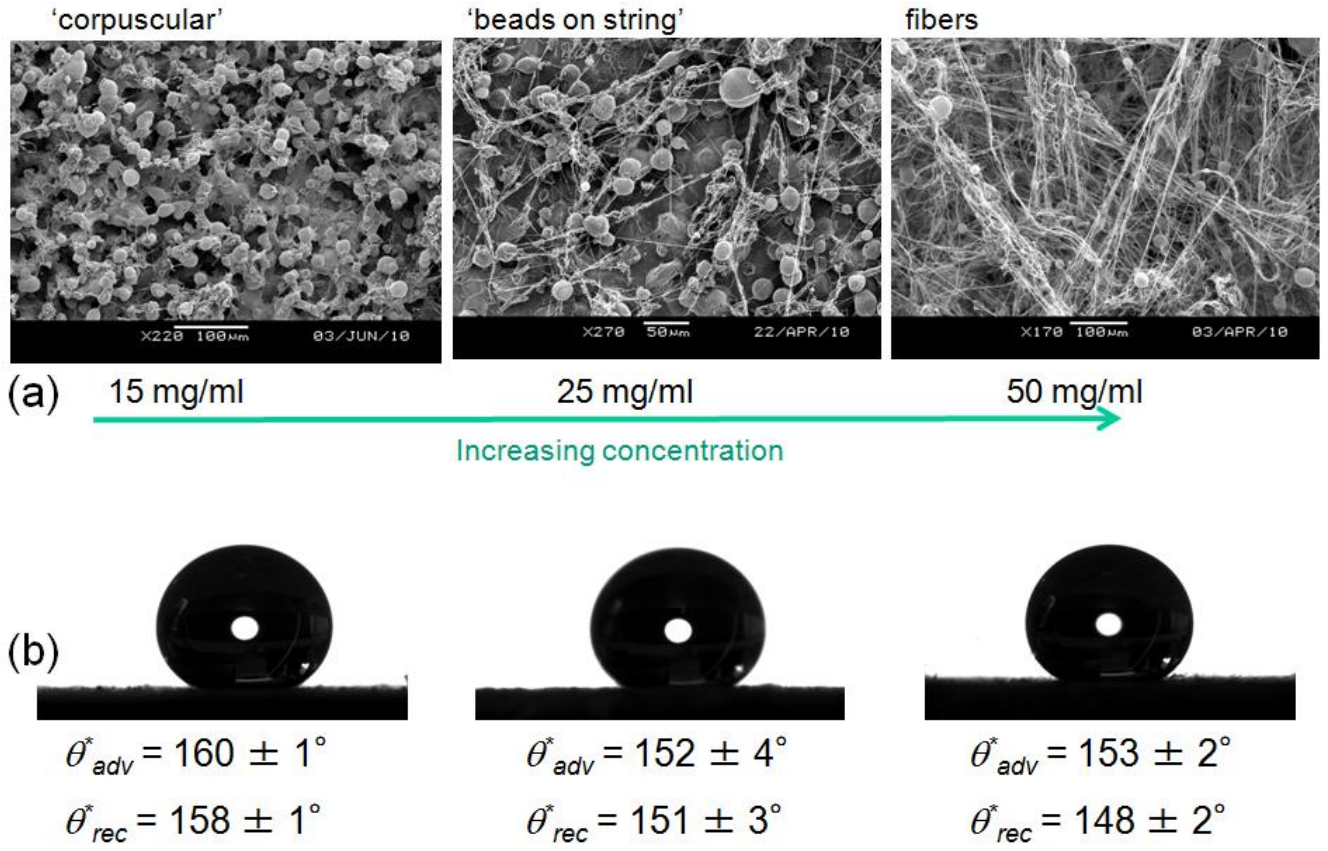

Figure 3 (a) Scanning electron microscope images of silicon surfaces sprayed with 50/50 wt% PMMA/flurodecyl POSS blends (B2; M_w=593k, PDI=2.69) of differing solute concentrations as indicated. **(b)** Droplets of water (V~ 15 μl) on each of the morphologies with corresponding values of apparent advancing (θ^*_{adv}) and receding (θ^*_{rec}) contact angles.

In the electrospinning process, the relative humidity of the atmosphere is an important parameter that can influence the fine topographic structure via the formation of porous surface features at large relative humidities (RH > 30%) [42]. In an analogous manner, SEM micrographs of individual spherical microbeads obtained in our spraying process at high relative humidities ($RH \approx 50\%$) reveal the existence of nanoporous surface features (Figure 4a). While the possible

mechanisms leading to the formation of these nanopores are complex [42], the nanoporous features serve to reduce the solid/liquid fraction (ϕ_s) and contribute to an additional scale of roughness, which may also serve to lower contact angle hysteresis [43]. At lower relative humidities ($RH \approx 20\%$), a fraction of the corpuscular microstructures are collapsed or shrunken (Figure 4b). However the regions containing these collapsed structures do not seem to measurably affect the overall non-wetting properties. The apparent advancing and receding contact angles with water were measured to be $\theta^*_{adv} = 160^\circ, \theta^*_{rec} = 158^\circ$ at $RH \approx 50\%$, and $\theta^*_{adv} = 160^\circ, \theta^*_{rec} = 159^\circ$ at $RH \approx 20\%$

.

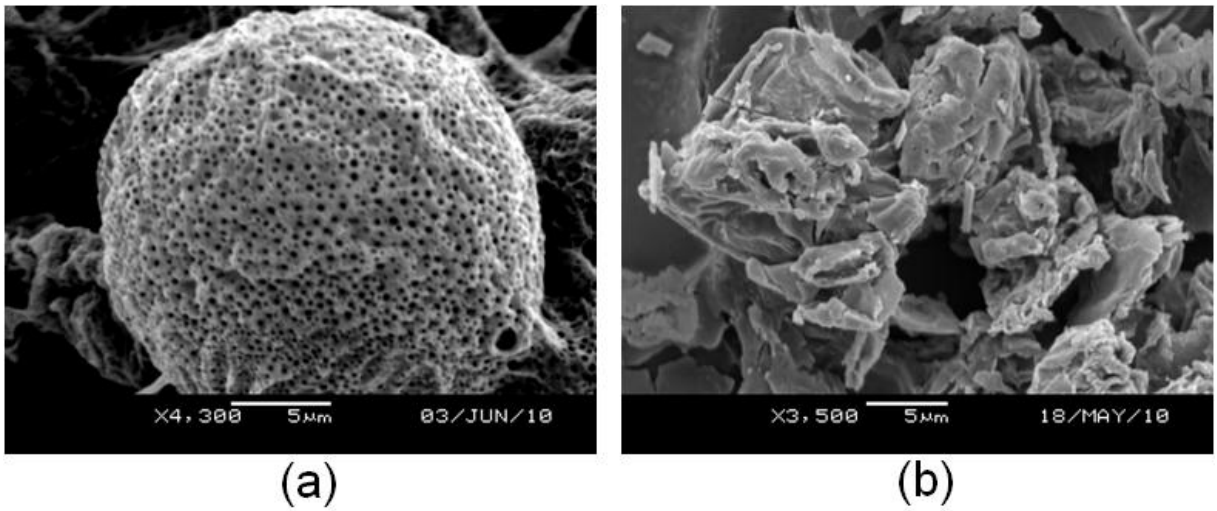

Figure 4. SEM images of individual corpuscular microtextures (B2; 50/50 POSS/PMMA blend; 15mg/ml) at **(a)** *RH*=51.3 %, $\theta^*_{adv} = 160^\circ, \theta^*_{rec} = 158^\circ$; **(b)** *RH*=23.7 %, $\theta^*_{adv} = 160^\circ, \theta^*_{rec} = 159^\circ$.

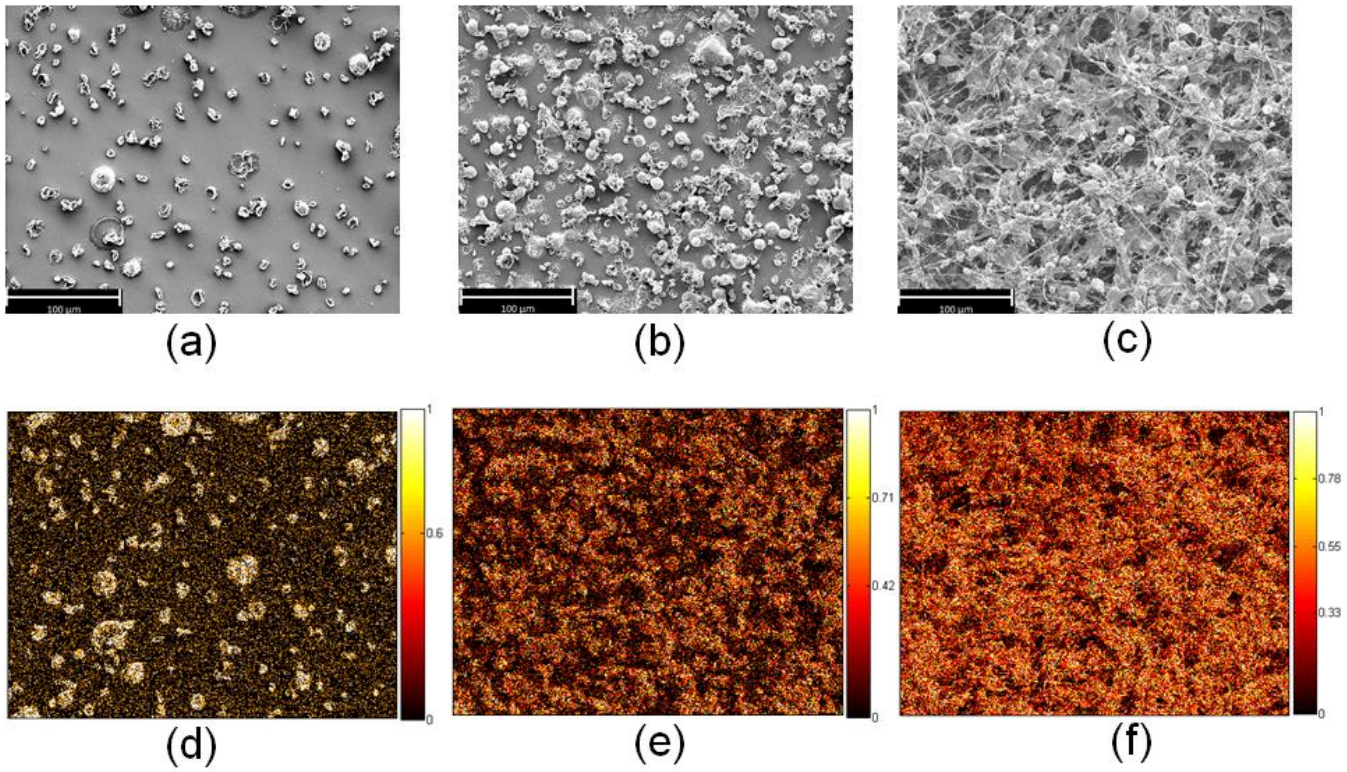

Figure 5. (a-c) SEM images of surface structures obtained upon spraying a 50/50 POSS/PMMA blend at 25 mg/ml and a working distance of 25 cm using low polydispersity PMMA standards (N1,N2,N3). The images show a transition from a sparse coverage (N1; Mw~124k g/mol), to a corpuscular structure (N2; Mw~272k g/mol), and finally to a beads on string structure (N3; Mw~761k g/mol) with increasing molecular weight. **(d-f)** The corresponding energy-dispersive X-ray spectroscopy (EDX) elemental map showing the spatial distribution of elemental fluorine. The fractional area coverage of fluorine, calculated from the pixel intensity of the EDX images, is 0.25, 0.39 and 0.62 in figures (d-f) respectively.

To investigate the impact of increasing molecular weight (M_w) of PMMA on the obtained surface texture, a series of monodisperse PMMA (PDI < 1.2)/fluorodecyl POSS 50/50 blends were sprayed at a constant solute concentration of 25 mg/ml at a distance of 25 *cm* and under a pressure of 170 *kPa*. Increasing M_w at this specific fixed concentration of polymer results in a transition from a corpuscular morphology (M_w=272,000 g/mol) to a beads-on-string morphology (M_w=761,000 g/mol), as seen in Figure 5a-c. Energy-dispersive X-ray spectroscopy (EDX) was simultaneously performed to determine the spatial distribution of elemental fluorine (Figure 5d-f) which corresponds to the distribution of flurodecyl POSS on the sprayed surface, averaged over a penentration depth of $\sim 1\,\mu m$. An estimate of the fractional area coverage of fluorine is obtained

from the EDX image as a ratio of the number of pixels indicating the presence of fluorine to the total number of pixels. At a low molecular weight (M_w=124,000 g/mol) the low viscosity of the solution results in insufficient surface coverage of the sprayed coating (Figure 5a) resulting in apparent contact angles that are lower than those obtained on a flat-spin coated surface $\left(\theta_E = 124^\circ\right)$ of the same polymer blend. As the molecular weight of the solute increases, the surface area coverage also increases. In Table 2 we summarize the relationship between the weight average molecular weight, the apparent contact angle, fluorine surface coverage and surface texture. The zero shear viscosities of the three blends are observed to increase with M_w as expected. The morphology of the surface systematically varies with increasing molecular weight and concentration, resulting ultimately in fiber formation, which is indicative of suppression of the break-up of the polymer jet during the spraying process. The specific morphological details, including the fraction of beads and fibers exhibited by the beads-on-string morphology, depend on features of the molecular weight distribution, and we are currently investigating this phenomenon.

In the corresponding electrospinning process, Shenoy *et al* [44] have developed a correlation that helps rationalize fiber formation in electrospinning due to increases in polymer molecular weight and concentration in terms of chain entanglement for polymer solutions that are in the good solvent limit with concentrations in the semi-dilute regime well above the critical overlap concentration $\left(c >> c^*\right)$. In Figure 6a, we provide an analogous operating diagram for the spraying process described in the present work. This plot maps the various microtextures obtained by spraying solutions of different M_w and c onto regions of parameter space that are above and below the coil overlap concentration c^*. The corresponding SEM micrographs are provided in the supplementary information (Figure A1). The behavior of PMMA in Asahiklin AK-225, a solvent containing isomers of dichloropentafluoropropane and used in the spraying experiments, has not been studied in detail. However, previous studies on the intrinsic viscosity behavior of PMMA show that CFCs and HCFCs act as good solvents [45]. In particular, the Mark-Houwink-Sakurada parameters experimentally evaluated for PMMA in 2,2,3,3-Tetrafluoropropanol by Hamori *et al* [46] $\left(K = 7.2\times10^{-3}\text{ml/g}; a = 0.79\right)$ are used in this study for the purpose of obtaining a theoretical estimate of the overlap concentration using the equation $c^* = 6^{3/2} M_w \Big/ 8N_A \left\langle R^2 \right\rangle^{3/2}$ [47]. Here N_A is Avogadro's number and $\left\langle R^2 \right\rangle = \alpha^2 C_\infty \left(2M_w/M_0\right) l^2$ is the mean-square end-to-end distance of the polymer coils, with the characteristic ratio for PMMA given by $C_\infty = 6.9$ and bond length $l = 1.54\times10^{-10} m$ [48]. The dependence of the Flory expansion factor α on the molecular weight is

obtained from the following expression $\alpha^3 \equiv [\eta]/[\eta_\theta] = (K/K_\theta) M^{a-1/2}$ [49], and the value of $K_\theta = 4.8\times10^{-4}$ ml/g for PMMA in a θ-solvent was experimentally obtained by Fox [50], and is independent of temperature in the range of $30^\circ C$ to 70°C. For the series of fairly monodisperse PMMA samples (N1-N4) used in the spraying experiments, the molecular weight in the Mark-Houwink-Sakurada expression can be taken to be $M \approx M_w$. Thus, the final expression for the estimate of the critical overlap concentration c^* can be written in terms of the weight-averaged molecular weight as:

$$c^* = 8.69\times10^5 \, M_w^{-0.79} \ (\text{mg/ml}) \qquad (2)$$

The dotted line in Figure 6a corresponding to equation (2) represents the predicted dependence of the overlap concentration (c^*) on molecular weight. The circles denote the morphology observed upon spraying pure PMMA (Samples N1-N4) in Asahiklin at a specific concentration and molecular weight. For moderate molecular weights ($M_w<10^6$ g/mol), a transition from corpuscular to fiber-containing structures is observed for $c/c^* \approx 1$, indicating the key role of chain overlap in stabilizing the fiber formation. At very high molecular weights (Sample N4 with M_w=2,276,000 g/mol), the extensional viscosity of even a dilute solution ($c/c^* < 1$) is large enough to stabilize the formation of submicron fibers [51, 52] for sufficiently long periods to enable the solvent to evaporate and the POSS/PMMA blend to solidfy as shown in Figure 6b.

Table 2. Numerical values of the molecular weights and polydispersity indices of the PMMA standards and the corresponding water contact angles and surface texture on the respective sprayed surfaces, along with the zero-shear viscosities of the corresponding polymer solution. The EDX fluorine intensity is calculated as the ratio of pixels in the EDX image indicating the presence of fluorine to the total number of pixels.

M_w (g/mol)	PDI	θ^*_{adv}	θ^*_{rec}	θ_E	Structure	EDX Fluorine Intensity	η (cP)
124,000	1.04	38	37	124	Sparse	0.25	1.2
272,000	1.11	159	157	124	Corpuscular	0.39	1.9
761,000	1.13	159	158	124	Beads on string	0.62	4

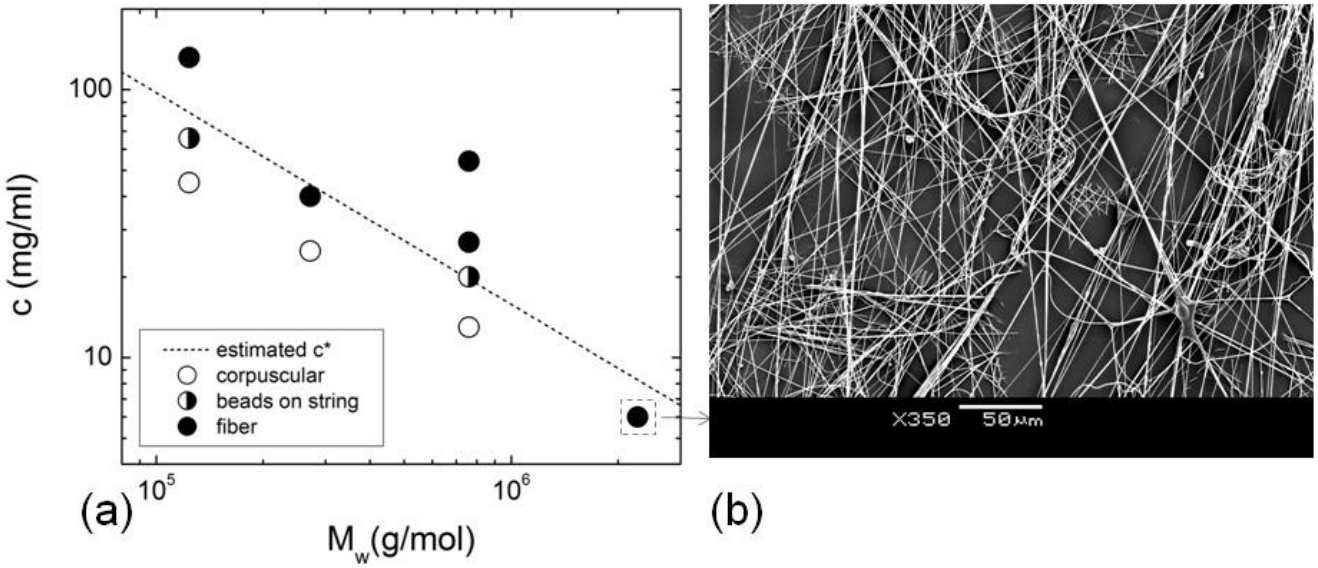

Figure 6.(a) Operating diagram for solution spraying of pure PMMA structures, showing the variation of the observed morphologies upon increasing the concentration of polymer solution for various molecular weights (M_w). The dotted line corresponds to equation (2), which describes the estimated semi-dilute overlap concentration (c^*) for PMMA as a function of M_w. **(b)** SEM image of

the fiber morphology upon spraying a dilute PMMA solution of c=6 mg/ml $\left(c/c^{*}=0.7\right)$ and very high molecular weight M_w=2,276,000 g/mol.

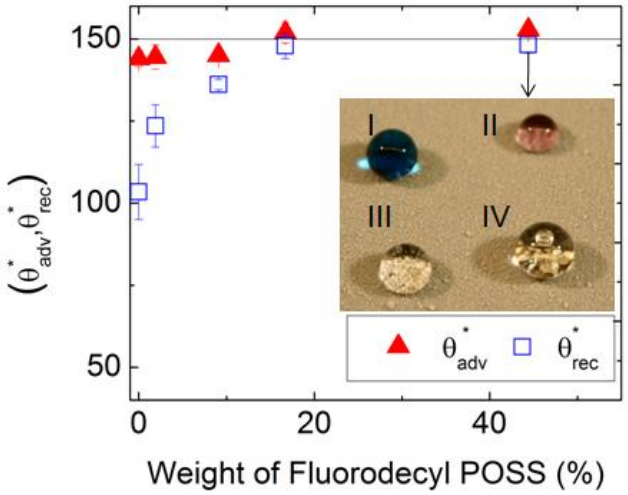

Figure 7. Advancing (θ^{*}_{adv}) and receding (θ^{*}_{rec}) water contact angles on a silicon substrate spray coated with 50 mg/ml PMMA (B2; M_w=593,000 g/mol, PDI=2.69)/fluorodecyl POSS blends of varying POSS fraction. Inset: Drops of I-Water, II-Ethanol, III-Decane, IV-Rapeseed oil displaying superoleophobic behavior

A potential application of these highly textured surfaces is the rapid and simple production of superomniphobic surfaces [23]. The weight fraction of fluorodecyl POSS in the POSS/PMMA blend is an important parameter in promoting the liquid repellency of the sprayed POSS/PMMA blends to low surface tension liquids. In Figure 7, we show the variation of the apparent water contact angles with POSS content on a fibrous surface prepared by spraying different weight fractions of a 50 mg/ml mixture of POSS/PMMA (B2; M_w = 593,000 g/mol, PDI = 2.69) for 15 seconds. An increase in the weight fraction of fluorodecyl POSS in the solution increases both the apparent advancing (θ^{*}_{adv}) and receding (θ^{*}_{rec}) water contact angles on the resulting sprayed surfaces, asymptoting to a maximum value of $\theta^{*}_{adv}=152^{\circ}\pm2^{\circ}, \theta^{*}_{rec}=148^{\circ}\pm2^{\circ}$ at 44.4 wt% fluorodecyl POSS, which is consistent with the previous work by Tuteja *et. al* [22] on electrospun POSS/PMMA surfaces. Concomitantly, the contact angle hysteresis ($\Delta\theta^{*}=\theta^{*}_{adv}-\theta^{*}_{rec}$) decreases as

the weight fraction of POSS increases, from $\Delta\theta^* = 39^\circ$ at 0 wt% fluorodecyl POSS to $\Delta\theta^* = 4^\circ$ at 44.4 wt% fluorodecyl POSS. While the large value of contact angle hysteresis at low POSS fractions (<10 wt%) is indicative of a sticky hydrophobic surface [53], the low hysteresis at high weight fractions of fluorodecyl POSS indicates the existence of a Cassie-Baxter state. For fluorodecyl POSS fractions greater than 16 wt%, a superhydrophobic surface (with $\theta^* > 150^\circ$ and $\Delta\theta^* < 5^\circ$) is obtained. In the inset of Figure 7, the oleophobic or omniphobic behavior of the sprayed surface at 44.4 wt% fluorodecyl POSS is demonstrated and the spray-on surface coating repels a wide range of liquids. This omniphobicity is further explored in Figure 8, where we show the measured advancing and receding contact angles for a series of liquids over a particular corpuscular surface prepared by spraying a 50 wt% mixture of POSS/PMMA (B1; c = 50 mg/ml, M_w = 102,000 g/mol, PDI = 1.56) on a flat silicon substrate. The surface exhibits liquid repellency over a range of liquid surface tensions. The highest observed apparent contact angle (θ^*_{adv}) with water (γ_{lv} = 72.8 mN/m) was 159° with a corresponding contact angle hysteresis $\Delta\theta^* = 2^\circ$. A variety of low surface tension oils including dimethyl sulfoxide (γ_{lv} = 43 mN/m), rapeseed oil (γ_{lv} = 35.5mN/m), hexadecane (γ_{lv} = 27.5 mN/m) and decane (γ_{lv} = 23.8 mN/m) exhibit superoleophobic behavior with advancing contact angles in excess of 150°. However, as seen in Figure 8a, the contact angle hysteresis progressively increases for liquids with lower surface tensions as the droplets experience an increasing number of pinning events on the highly textured spray-coated surface [43]. The sliding angle (ω), defined here as the angle of the tilt stage at which the liquid drop rolls off the surface without leaving any residual trail, is measured at a constant drop volume of $V = 10\mu l$ for different liquids, and is shown in Figure 8b. The measured sliding angles are compared with the predicted values for the contact angle hysteresis calculated using the Extrand-Gent model [54-56] which can be written in the form $\sin(\omega) = \left(\frac{2\gamma_{lv} d}{\pi\rho g V}\right)\left(\cos\theta^*_{rec} - \cos\theta^*_{adv}\right)$. Here d corresponds to the diameter of the droplet at the triple phase contact line and V is the volume of the drop. The diameter of the triple phase contact line was directly measured from the computer image of the drop. The measured values of the sliding angle are larger than the predicted value evaluated from the Extrand-Gent model, as seen in Figure 8b. This is again indicative of pinning of the receding contact line on the local features of the microtextured surface [55]. The relatively large roll-off angle and high contact angle hysteresis for decane ($\Delta\theta^* = 41^\circ \pm 16^\circ, \omega = 37^\circ \pm 2^\circ$) can be attributed to a partial localized wetting of the surface suggesting the incipient transition to a fully wetted interface. Heptane (γ_{lv} = 20.1 mN/m) fully wets the surface resulting in a very low apparent contact angle $\left(\theta^*_{adv} = 51^\circ \pm 13^\circ \text{ and } \theta^*_{rec} \approx 0^\circ\right)$, marking

a complete transition to the Wenzel regime. The Cassie-Baxter state is metastable for many low surface tension liquids and a pressure perturbation might cause an irreversible transition into the fully wetted state [23]. In order to estimate the robustness against a pressure-induced wetting transition to the Wenzel state when water is the contacting liquid, a simple immersion test was conducted in which the substrate was immersed in a column of water. The substrate which was spray coated with a 44.4 wt% POSS/PMMA (B1; M_w = 102,000 g/mol, PDI = 1.56, c = 50 mg/ml) blend retained its non-wettability through the entire height of the column, which corresponds to a maximum static pressure of 4410 Pa (h=45 cm). The presence of a plastron film, a silvery mirror-like reflecting interface due to a trapped layer of air verified the Cassie-Baxter composite interface. (See supplementary Information Figure A2)

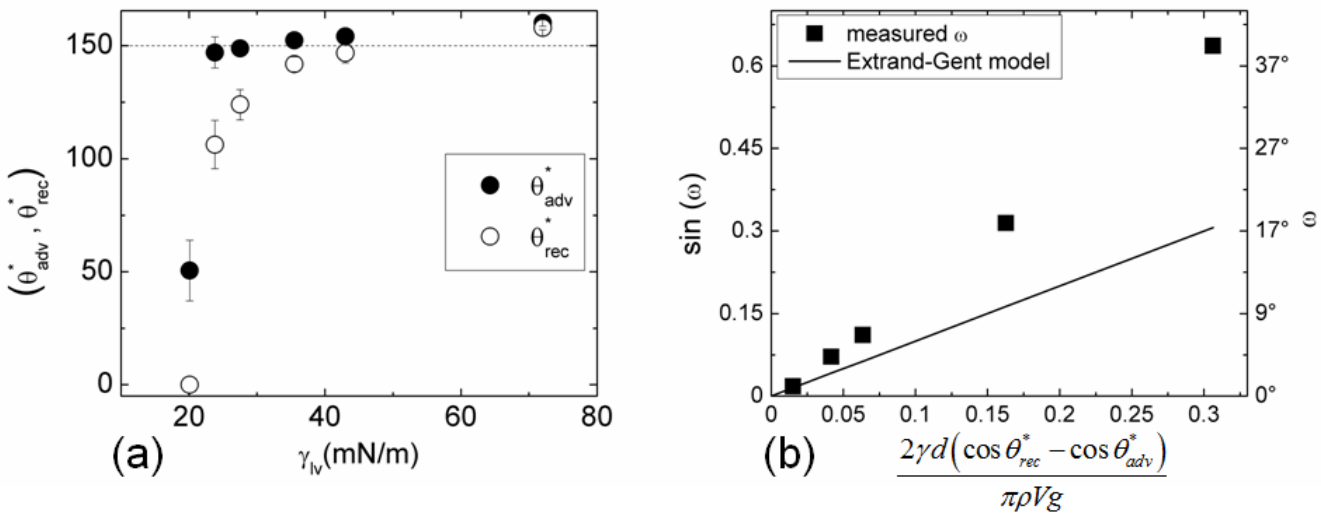

Figure 8 (a) Measured values of the apparent advancing (θ^*_{adv}) and receding (θ^*_{rec}) contact angles with water (γ_{lv} = 72.8 mN/m), dimethyl sulfoxide (γ_{lv} = 43 mN/m), rapeseed oil (γ_{lv} = 35.5 mN/m), hexadecane (γ_{lv} = 27.5 mN/m), decane (γ_{lv} = 23.8 mN/m) and n-heptane (γ_{lv} = 20.1 mN/m) liquid drops of volume ~ 10 µl on a surface spray coated with 50/50 fluorodecyl POSS/PMMA (B1; PDI = 1.56, M_w = 102,000 g/mol). The dashed line represents the boundary of the super-nonwetting regime. **(b)** The measured sliding angle (ω) is plotted against the predicted sliding value from the Extrand-Gent model evaluated using the corresponding values of θ^*_{adv} and θ^*_{rec}, represented by the solid line.

The omniphobic behavior of the sprayed surfaces shown in Figures 7 and 8 is a consequence of a surface topography with pronounced re-entrant surface curvature [22] as evidenced from the scanning electron micrographs in Figure 3. The presence of re-entrant features, in the form of spherical microbeads and cylindrical fibers [57], allows the liquid-air interface to locally satisfy the Young equation at numerous points along the strongly curved substrate features, and this facilitates the existence of the Cassie-Baxter state for low surface tension liquids [23, 39, 58]. The different morphologies formed during the solution spraying technique (Figure 3), are nearly identical to structures obtained by electrospinning similar PMMA/fluorodecyl POSS solutions [23]. A clear advantage of the spraying technique is the ability to reproduce and tailor surface morphologies in the absence of the very strong electric field required for electrospinning.

The microstructures which are formed during the solution spraying process are randomly oriented over large length scales, and the average feature size sampled by a microliter scale liquid drop placed on one of these surfaces is not immediately apparent from existing micrographs such as Figure 3 or Figure 5. The influence of the surface texture of the sprayed surfaces on wettability can be characterized by using an appropriate measure of the surface texture captured in the Cassie-Baxter equation (Eq. 1). This can be determined by regressing experimental contact angle measurements with the corresponding theoretical prediction. An idealized geometrical model for the corpuscular beads and fibrous mesh is used to characterize the randomly oriented surface geometry in terms of a single dimensionless feature spacing parameter (D^*) [57, 59]. The fiber-dominated geometries are approximated as an array of uniform cylinders of diameter 2*R*, which are spaced a distance *2D* apart and the surfaces composed of corpuscular beads are modeled as hexagonally packed spheres of diameter 2*R*, with a spacing distance of *2D* (Figure 9). For the cylindrical model, the Cassie-Baxter equation can then be written as [23, 59-62]

$$\cos\theta^* = -1 + \frac{1}{D^*}\left[(\pi - \theta_E)\cos\theta_E + \sin\theta_E\right] \tag{3}$$

where $D^* = (R+D)/R$, $r_\phi = (\pi - \theta_E)/\sin\theta_E$ and $\phi_s = \sin\theta_E / D^*$. For the model of hexagonally packed spheres, the relevant Cassie-Baxter equation is [59]:

$$\cos\theta^* = -1 + \frac{1}{D^*}\left[\frac{\pi}{2\sqrt{3}}(1+\cos\theta_E)^2\right] \tag{4}$$

where $D^* = \left[(R+D)/R\right]^2$, $r_\phi = 2(1+\cos\theta_E)/\sin^2\theta_E$ and $\phi_s = \pi\sin^2\theta_E / 2\sqrt{3}D^*$. For these model geometries, the fraction of the liquid in contact with the solid, $r_\phi\phi_s$ scales inversely with the spacing ratio D^*. In Figure 9, we show a non-wetting diagram [34, 63] in which we represent the cosine of the apparent advancing (θ^*_{adv}) contact angles measured with a series of liquids of varying surface tension as a function of the corresponding advancing contact angles (θ_{adv}) measured on smooth spin-coated silicon wafer surfaces. The enhanced liquid repellency of the structured surfaces is apparent from the large (negative) values of $\cos\theta^*_{adv}$ that can be obtained even when the contact angle of the liquid on the corresponding flat surface is less than 90°. The effective or average value of spacing ratio D^* is calculated by fitting the simplified Cassie-Baxter equation for each data set and corresponding model, and we find $D^* = 6.1 \pm 0.5$ for the fibrous mesh and $D^* = 9.0 \pm 1.2$ for the corpuscular structures. The Cassie-Baxter states that sit in the fourth quadrant ($\theta_A < \pi/2,\ \pi/2 < \theta^*_A < \pi$) are inherently metastable to sufficiently large pressure perturbations

[23, 61]. As the surface tension of the wetting liquid is progressively decreased, the magnitude of the energy barrier between the Cassie-Baxter and Wenzel state decreases [58], and eventually a droplet of heptane (γ_{lv}=20.1 mN/m) transitions spontaneously to a fully wetted Wenzel state even under equilibrium/rest conditions for either of the textured surfaces.

Prior to the wetting transition it is clear that the simple models given by Eq. (3), Eq. (4) can accurately capture the evolution in the apparent contact angle for the microtextured surfaces formed by spraying the polymer/POSS solutions, in agreement with earlier experiments performed using ideal dipcoated meshes [59]. The larger value of D^* obtained for the corpuscular surfaces reflect the lower fraction of solid substrate that is in wetted contact with the drop and the correspondingly higher value of the apparent contact angles that are obtained.

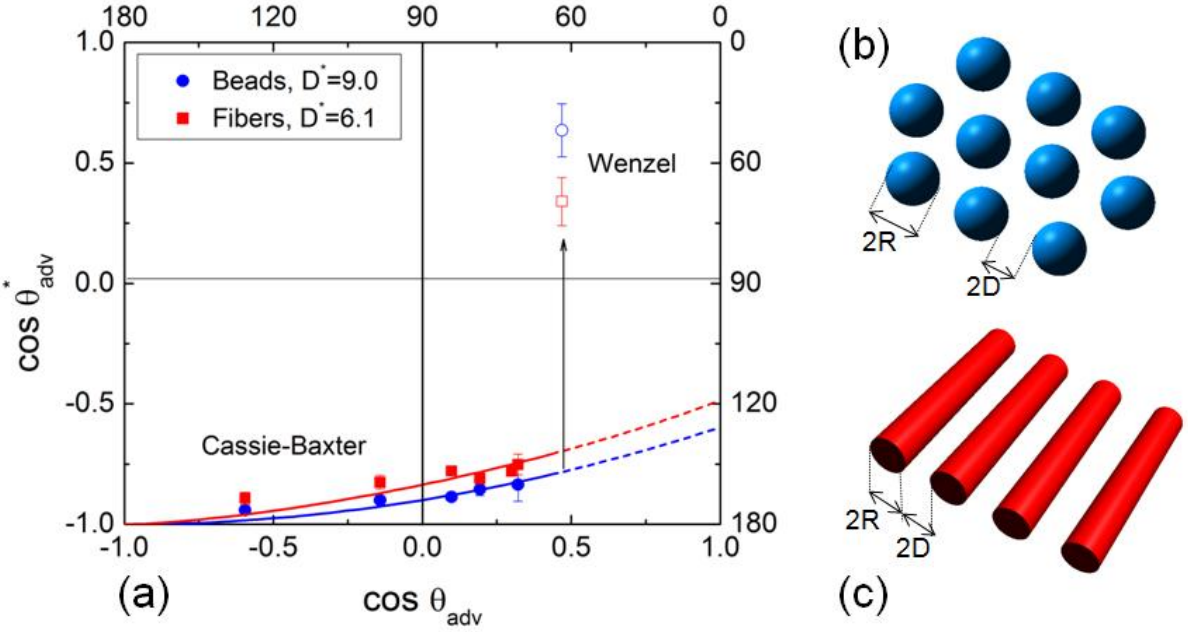

Figure 9 (a) The cosine of the apparent advancing contact angle (θ^*_{adv}) measured on the corpuscular (●) and fibrous (■) sprayed surface plotted against the corresponding cosine of the advancing contact angle (θ_{adv}) on a homogenous smooth spin-coated surface. The contacting liquids used are water (γ_{lv} = 72.8 mN/m), dimethyl sulfoxide (γ_{lv} = 43 mN/m), rapeseed oil (γ_{lv} =35.5 mN/m), hexadecane (γ_{lv} = 27.5 mN/m), dodecane (γ_{lv} = 25.4 mN/m) and decane (γ_{lv} = 23.8 mN/m). The solid line represents the best fit for the Cassie-Baxter equation used to obtain estimates of the dimensionless geometrical spacing ratio $\left(D^*\right)$ that characterize the randomly textured surfaces. A transition to the Wenzel regime (represented by the arrow) is observed for a droplet of heptane (γ_{lv} = 20.1 mN/m). **(b,c)** Schematics of a system of hexagonally packed spheres used to model the corpuscular surface, and an array of cylinders used to model the fibrous surface.

As already mentioned above, the similarity of these structures to those produced by electrospinning [41] is noteworthy. Electrospinning is a process which has been used widely to fabricate textured surfaces and non-woven fabrics by accelerating the spinning of a thin jet of polymeric fluid via action of electrostatic forces [64]. The electrohydrodynamic instability of the slender fluid jet determines the surface morphologies obtained on the collector plate, and a beads-on-string or corpuscular structure is obtained when the elongational stresses in the jet are unable to fully suppress the Rayleigh instability mechanism of jet break-up [51]. The filament thinning and break up of viscoelastic fluid jets are governed by different physical processes involving inertio-capillary, viscous and elastic forces. The relative importance of these forces can be determined in terms of two dimensionless parameters defined as the ratios of the time scales characterizing each process [65, 66]. The Ohnesorge number (*Oh*) is defined as the ratio of the viscous time scale $t_\eta \sim \eta_0 l/\gamma_{lv}$ and the inertial or Rayleigh time scale [67] $t_R \sim \sqrt{\rho l^3/\gamma_{lv}}$ to give $Oh = t_\eta / t_R = \eta_0 / \sqrt{\rho \gamma_{lv} l}$ where η_0 is the zero shear viscosity and l is the characteristic length scale of the flow, which is here taken to be the nozzle diameter. While the Ohnesorge number defined above provides an estimate of the role of viscous stresses, the relative importance of elastic stresses in stabilizing fiber production can be estimated from an intrinsic Deborah number [65], $De \sim \lambda / \sqrt{\rho l^3 / \gamma_{lv}}$, defined as a ratio of the polymer relaxation time scale $t_p \sim \lambda$ and the Rayleigh time scale t_R. A theoretical estimate of the longest relaxation time λ can be obtained using the non-free draining limit of the Zimm theory for a flexible polymer chain dissolved in a good solvent using the expression $\lambda_{zimm} \approx ([\eta] M_w \eta_s) / (N_A k_B T)$ [68], where $\eta_s = 0.59$ cP is the solvent viscosity, N_A is Avogadro's number, k_B is the Boltzmann constant, T is the absolute temperature, $[\eta] = KM^a = 7.2 \times 10^{-3} M_w^{0.79}$ ml/g is the intrinsic viscosity of the PMMA/hydrofluorocarbon solvent system taken from the Mark-Houwink-Sakurada expression determined by Hamori *et al* [46] and applied to the monodisperse PMMA samples dissolved in Asahiklin. In Table 3, we list the longest (Zimm) relaxation time, the Ohnesorge number (*Oh*) and the Deborah number (*De*) calculated for different fluorodecyl POSS/polymer solutions and the corresponding morphologies obtained. The longest estimated relaxation time for the PMMA/solvent system increases by over two orders of magnitude over the range of molecular weights used, from $\lambda_z \sim 1 \mu s$ for M_w=124,000 g/mol to $\lambda_z \sim 410 \mu s$ for M_w=2,276,000 g/mol, which coincides with the appearance of fibrous morphologies upon spraying. The uniformly low value of the Ohnesorge number

throughout the range of PMMA/solvent conditions studied in the present work signifies the negligible contribution of viscous stresses towards stabilizing fiber formation, which along with the significant increase in the relaxation time and Deborah number, indicate that the morphologies produced by simple solution spraying are due to increasing viscoelastic effects progressively retarding the jet break up phenomenon and promoting the formation of fibers.

A dilute solution of very high molecular weight (N4; M_w=2,276,000 g/mol) and low PMMA concentration c=6mg/ml ($c/c^* = 0.7$) was also observed to produce fibers upon spraying (Figure 6b), indicating that it is not under coil overlap near equilibrium conditions per se that leads to these features but the increased elongational viscosity of very dilute polymer solution at high molecular weights which contributes to the suppression of jet break up during the spraying process. The critical role of the high M_w polymer in the suppression of jet break-up is also evidenced in Figure 10, where we show the influence of adding a small fraction of high molecular weight PMMA to a non-spinnable solution of low M_w PMMA resulting in the formation of a fibrous morphology. A blend of 96% low M_w PMMA (B1; M_w=102,000 g/mol) and 4% high M_w PMMA (N4; Mw=2,276,000 g/mol) sprayed at a concentration of c=50 mg/ml is seen to produce fibrous structures, while a similar concentration (c/c^*=0.75**,** c=45 mg/ml) of the pure low M_w PMMA produces corpuscular structures.

Table 3 Values for the longest relaxation times obtained from the Zimm theory (λ_{zimm}), and for the Ohnesorge (Oh) and Deborah (De) numbers that characterize the relative importance of viscous and elastic effects respectively, for fluorodecyl POSS/PMMA solutions of varying concentrations and molecular weights.

$M_w(\times 10^3)$ (g/mol)	$\frac{c}{c^*}$	$\lambda_{zimm}(\mu s)$	Oh	De	Structure
124	0.26	1.6	1.2×10^{-2}	7.1×10^{-4}	Sparse
272	0.57	9.2	2.0×10^{-2}	4.1×10^{-3}	Corpuscular
761	1.04	58	4.1×10^{-2}	2.6×10^{-2}	Beads on string
2276	0.72	410	1.7×10^{-2}	1.8×10^{-1}	Fibers

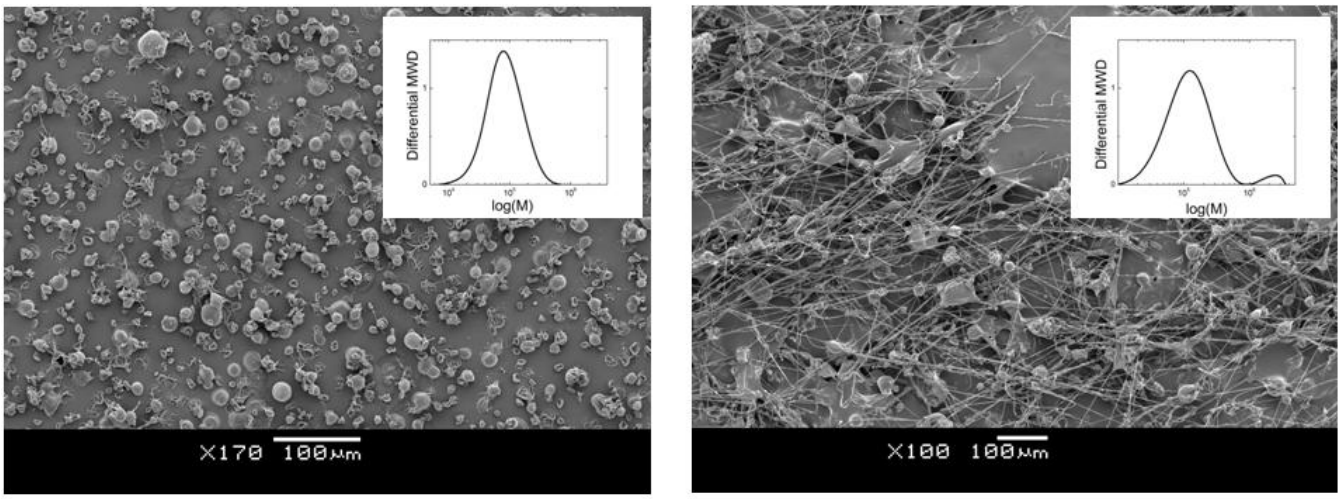

Figure 10 SEM images of microstructures obtained on spraying **(a)** pure PMMA (B1; c/c^*=0.75, c=45 mg/ml, M_w=102k g/mol) **(b)** blend of 4% high M_w PMMA (N4; M_w=2276k g/mol) + 96% low M_w PMMA (B1; M_w=102k g/mol) at a concentration c=50 mg/ml. The inset in the SEM images shows the GPC curves corresponding to the pure PMMA and the blend of high and low M_w PMMA respectively.

IV. Conclusion

A simple spraying technique that enables fabrication of microtextured surfaces from a polymer solution has been demonstrated. The surface morphology observed in SEM images ranged from randomly dispersed spherical microbeads or corpuscular structures to bundled fibers and can be controlled systematically by varying the solute concentration and the polymer molecular weight. Studies with a wide range of polymer molecular weights show that the critical concentration or coil overlap (c^*) provides a good estimate of the critical conditions for the formation of fibrous microstructures, except at very high molecular weights when even dilute polymer solutions $\left(c < c^*\right)$ are spinnable due to the high elongational viscosity of the dilute solution. The incorporation of the low surface energy 1H,1H,2H,2H-heptadecafluorodecyl polyhedral oligomeric silsesquioxane (fluorodecyl POSS) cage molecules confers the sprayed POSS/PMMA surface coatings with enhanced liquid repellency. The surface repellency was characterized by measuring the apparent advancing, receding and roll-off angles, and superomniphobic behavior was observed for liquids with a wide range of liquid surface tensions. Idealized geometrical models for the resulting textures were used to evaluate a characteristic dimensionless spacing ratio (D^*) that parameterized the surface morphology obtained from the solution spraying process. The larger value of $D^* = 9.0 \pm 1.2$ obtained for the corpuscular structures when compared to the bundled fibers

($D^* = 6.1 \pm 0.5$) reflects the correspondingly higher values of apparent contact angle obtained on the corpuscular structures for a range of liquid surface tensions.

A number of simple solution spinning and spraying techniques have recently been described for preparation of textured and hydrophobic surfaces [10, 30, 31]. The ability to control the morphology of the microtextures and the weight fraction of fluorodecyl POSS deposited on the surface using our solution spraying process enables us to systematically control the oleophobicity and contact angle hysteresis of the coating that is applied to a substrate. The simplicity of the solution spraying process used in the present study is particularly helpful in facilitating rapid and cheap production of omniphobic coatings that can be applied over a large area. The re-entrant topographic features of these textured coatings promote establishment of Cassie-Baxter states in which microscopic pockets of air are trapped within the micro-texture resulting in high contact angles, low roll off angles and low hysteresis. The resulting textured and omniphobic surfaces may ultimately find utility as simple coatings that can be applied over a wide area for reducing frictional drag, ice adhesion or biofouling.

ACKNOWLEDGMENT

We acknowledge financial support from the Army Research Office (ARO) through Contract W911NF-07-D-0004, as well as the Air Force Research Laboratory, Propulsion Directorate, Air Force Office of Scientific Research. We thank Prof. Michael F. Rubner and the Institute for Soldier Nanotechnologies at MIT for the use of various laboratory facilities, Jonathan DeRocher for assistance with the spraying apparatus and safety overview, Thomas Ober for assistance with the rheometric characterization, and Dr. Vivek Sharma and Dr. Adam Meuler for helpful discussions during the preparation of this manuscript.

Supporting Information Available

SEM images corresponding to spraying polymer solutions of varying c and M_w, Image showing plastron formation and robustness to pressure-induced Wenzel transition, shear viscosity data for polymer solutions in Table 1, Image showing adhesion test of sprayed surface to silicon substrate according to ASTM D-3359 standard.

REFERENCES

1. Jayaraman K, Kotaki M, Zhang YZ, Mo XM, and Ramakrishna S. Journal of Nanoscience and Nanotechnology 2004;4(1-2):52-65.
2. Yang F, Murugan R, Wang S, and Ramakrishna S. Biomaterials 2005;26(15):2603-2610.
3. Burger C, Hsiao BS, and Chu B. Annual Review of Materials Research 2006;36:333-368.
4. Verreck G, Chun I, Rosenblatt J, Peeters J, Van Dijck A, Mensch J, Noppe M, and Brewster ME. Journal of Controlled Release 2003;92(3):349-360.
5. Ma ML, Gupta M, Li Z, Zhai L, Gleason KK, Cohen RE, Rubner MF, and Rutledge GC. Advanced Materials 2007;19(2):255-259.
6. Fisher RJ and Denn MM. AIChE Journal 1976;22(2):236-246.
7. Grafe T and Graham K. Nonwoven Technol Rev 2003:51–55.
8. Ellison CJ, Phatak A, Giles DW, Macosko CW, and Bates FS. Polymer 2007;48(11):3306-3316.
9. Wang D, Sun G, and Chiou B-S. Macromolecular Materials and Engineering 2007;292(4):407-414.
10. Medeiros ES, Glenn GM, Klamczynski AP, Orts WJ, and Mattoso LHC. Journal of Applied Polymer Science 2009;113(4):2322-2330.
11. Shiu JY, Kuo CW, Chen P, and Mou CY. Chem. Mater 2004;16(4):561-564.
12. Shirtcliffe NJ, McHale G, Newton MI, and Perry CC. Langmuir 2003;19(14):5626-5631.
13. Ma M, Hill RM, Lowery JL, Fridrikh SV, and Rutledge GC. Langmuir 2005;21(12):5549-5554.
14. Li M, Zhai J, Liu H, Song Y, Jiang L, and Zhu D. J. Phys. Chem. B 2003;107(37):9954-9957.
15. Lau KKS, Bico J, Teo KBK, Chhowalla M, Amaratunga GAJ, Milne WI, McKinley GH, and Gleason KK. Nano Letters 2003;3(12):1701-1705.
16. Leng BX, Shao ZZ, de With G, and Ming WH. Langmuir 2009;25(4):2456-2460.
17. Ahuja A, Taylor JA, Lifton V, Sidorenko AA, Salamon TR, Lobaton EJ, Kolodner P, and Krupenkin TN. Langmuir 2008;24(1):9-14.
18. Cao L, Price TP, Weiss M, and Gao D. Langmuir 2008;24(5):1640-1643.
19. Tsujii K, Yamamoto T, Onda T, and Shibuichi S. Angewandte Chemie International Edition in English 1997;36(9):1011-1012.
20. Yabu H, Takebayashi M, Tanaka M, and Shimomura M. Langmuir 2005;21(8):3235-3237.
21. Zimmermann J, Rabe M, Artus GRJ, and Seeger S. Soft Matter 2008;4(3):450-452.
22. Tuteja A, Choi W, Ma M, Mabry JM, Mazzella SA, Rutledge GC, McKinley GH, and Cohen RE. Science 2007;318(5856):1618.
23. Tuteja A, Choi W, Mabry JM, McKinley GH, and Cohen RE. Proceedings of the National Academy of Sciences 2008;105(47):18200.
24. Xi J, Feng L, and Jiang L. Applied Physics Letters 2008;92:053102.

25. Wang D, Wang X, Liu X, and Zhou F. The Journal of Physical Chemistry C 2010;114(21):9938-9944.
26. Yang J, Zhang Z, Men X, Xu X, and Zhu X. Langmuir 2010;26(12):10198-10202.
27. Yang J, Zhang Z-Z, Men X-H, and Xu X-H. Journal of Macromolecular Science, Part A: Pure and Applied Chemistry 2009;46(10):997 - 1000.
28. Bayer IS, Tiwari MK, and Megaridis CM. Applied Physics Letters 2008;93(17):173902-173903.
29. Bayer IS, Steele A, Martorana PJ, Loth E, and Miller L. Applied Physics Letters 2009;94(16):163902-163903.
30. Manoudis PN, Karapanagiotis I, Tsakalof A, Zuburtikudis I, and Panayiotou C. Langmuir 2008;24(19):11225-11232.
31. Steele A, Bayer I, and Loth E. Nano Letters 2008;9(1):501-505.
32. Lafuma A and Quéré D. Nature Materials 2003;2(7):457-460.
33. Marmur A. Langmuir 2004;20(9):3517-3519.
34. Quéré D. Annual Review of Materials Research 2008;Vol. 38:71-99.
35. Callies M and Quéré D. Soft Matter 2005;1(1):55-61.
36. Wenzel RN. Industrial & Engineering Chemistry 1936;28(8):988-994.
37. Cassie ABD and Baxter S. Transactions of the Faraday Society 1944;40:546-551.
38. Marmur A. Langmuir 2003;19(20):8343-8348.
39. Nosonovsky M. Langmuir 2007;23(6):3157-3161.
40. Mabry JM, Vij A, Iacono ST, and Viers BD. Angewandte Chemie-International Edition 2008;47(22):4137-4140.
41. Ma M, Mao Y, Gupta M, Gleason KK, and Rutledge GC. Macromolecules 2005;38(23):9742-9748.
42. Casper CL, Stephens JS, Tassi NG, Chase DB, and Rabolt JF. Macromolecules 2004;37(2):573-578.
43. Gao L and McCarthy TJ. Langmuir 2006;22(14):6234-6237.
44. Shenoy SL, Bates WD, Frisch HL, and Wnek GE. Polymer 2005;46(10):3372-3384.
45. Wagner HL. Journal of Physical and Chemical Reference Data 1987;16(2):165-173.
46. Hamori E, Prusinowski LR, Sparks PG, and Hughes RE. The Journal of Physical Chemistry 1965;69(4):1101-1105.
47. Graessley WW. Polymer 1980;21(3):258-262.
48. Flory PJ. Statistical mechanics of chain molecules: Interscience Publishers, 1969.
49. Flory PJ. Principles of polymer chemistry: Cornell University Press, 1953.
50. Fox TG. Polymer 1962;3:111-128.

51. Yu JH, Fridrikh SV, and Rutledge GC. Polymer 2006;47(13):4789-4797.
52. Bhat PP, Appathurai S, Harris MT, Pasquali M, McKinley GH, and Basaran OA. Nat Phys 2010;6(8):625-631.
53. Reyssat M and Quéré D. The Journal of Physical Chemistry B 2009;113(12):3906-3909.
54. Extrand CW and Gent AN. Journal of Colloid and Interface Science 1990;138(2):431-442.
55. Choi W, Tuteja A, Mabry JM, Cohen RE, and McKinley GH. Journal of Colloid and Interface Science 2009;339(1):208-216.
56. Furmidge CGL. Journal of Colloid Science 1962;17(4):309-324.
57. Tuteja A, Choi W, McKinley GH, Cohen RE, and Rubner MF. MRS bulletin 2008;33(8):752-758.
58. Marmur A. Langmuir 2008;24(14):7573-7579.
59. Chhatre SS, Choi W, Tuteja A, Park K-C, Mabry JM, McKinley GH, and Cohen RE. Langmuir 2009;26(6):4027-4035.
60. Michielsen S and Lee HJ. Langmuir 2007;23(11):6004-6010.
61. Chhatre SS, Tuteja A, Choi W, Revaux Al, Smith D, Mabry JM, McKinley GH, and Cohen RE. Langmuir 2009;25(23):13625-13632.
62. Choi W, Tuteja A, Chhatre S, Mabry JM, Cohen RE, and McKinley GH. Advanced Materials 2009;21(21):2190-2195.
63. Onda T, Shibuichi S, Satoh N, and Tsujii K. Langmuir 1996;12(9):2125-2127.
64. Shin YM, Hohman MM, Brenner MP, and Rutledge GC. Applied Physics Letters 2001;78(8):1149-1151.
65. Oliveira MSN, Yeh R, and McKinley GH. Journal of Non-Newtonian Fluid Mechanics 2006;137(1-3):137-148.
66. Ardekani AM, Sharma V, and McKinley GH. Journal of Fluid Mechanics 2010;665:46-56.
67. Rayleigh L. Proceedings of the London Mathematical Society 1878;s1-10(1):4-13.
68. Tirtaatmadja V, McKinley GH, and Cooper-White JJ. Physics of Fluids 2006;18(4):043101-043118.

Electronic Supplementary Material (online publication only)

Click here to download Electronic Supplementary Material (online publication only): Electronic_Supplementary_Information.doc